

RESEARCH ARTICLE

A unified theory on gravity current, interfacial and unsaturated flows in heterogeneous porous layers

Zhong Zheng^{1,2} 

¹State Key Laboratory of Ocean Engineering, School of Ocean and Civil Engineering, Shanghai Jiao Tong University, Shanghai, PR China

²MOE Key Laboratory of Hydrodynamics, School of Ocean and Civil Engineering, Shanghai Jiao Tong University, Shanghai, PR China

Corresponding author: Zhong Zheng; Emails: zzheng@alumni.princeton.edu; zhongzheng@sjtu.edu.cn

Received: 5 December 2024; **Revised:** 28 January 2025; **Accepted:** 25 March 2025

Keywords: heterogeneity; interfacial and unsaturated flow; wetting and capillary effects

Abstract

We provide a unified theory, within the framework of the multi-phase Darcy description, on gravity current, interfacial and unsaturated flows in a vertically heterogeneous porous layer, which finds applications in many geophysical, environmental and industrial contexts. Based on the assumption of vertical gravitational-capillary equilibrium, a theoretical model is presented to describe the time evolution of the saturation field and the interface shape, imposing a general formula for the vertical distribution of intrinsic permeability, porosity and capillary entry pressure. Example calculations are then provided in the Cartesian configuration to illustrate potential implications of the theory, imposing power-law distribution of vertical heterogeneity. Seven dimensionless parameters are identified, which arise from the standard Darcy description of multi-phase flow and measure the influence of vertical heterogeneity, viscosity ratio, and the competition between gravitational and capillary forces. Four asymptotic regimes are recognised, representing unconfined unsaturated flows, confined unsaturated flows, unconfined interfacial flows and confined interfacial flows. The influence of heterogeneity is then discussed in the two unsaturated flow regimes based on the evolution of the interface shape, frontal location, saturation distribution, and the time transition between unconfined and confined self-similar flows.

Impact Statement

Gravity current, interfacial and unsaturated flows find applications in many geophysical, environmental and industrial contexts, including geological CO₂ sequestration, groundwater migration, drainage and irrigation, pollutant transport, and enhanced recovery of crude oil. Many previous studies deal with different flow behaviours in homogeneous porous layers. In the present work, we focus on the influence of vertical heterogeneity, a common feature of sedimentary porous rocks, and arrive at a unified description for the propagation of gravity current, interfacial and unsaturated flows within a porous layer subject to fluid injections. The model leads to asymptotic and numerical solutions for the time evolution of the interface shape, frontal location, and the saturation distribution of both the invading and the ambient fluids, which could be valuable information in practical applications.

1. Introduction

Gravity current, interfacial and unsaturated flows find applications in many geophysical, environmental and industrial contexts. For example, such flows are closely related to the displacement processes



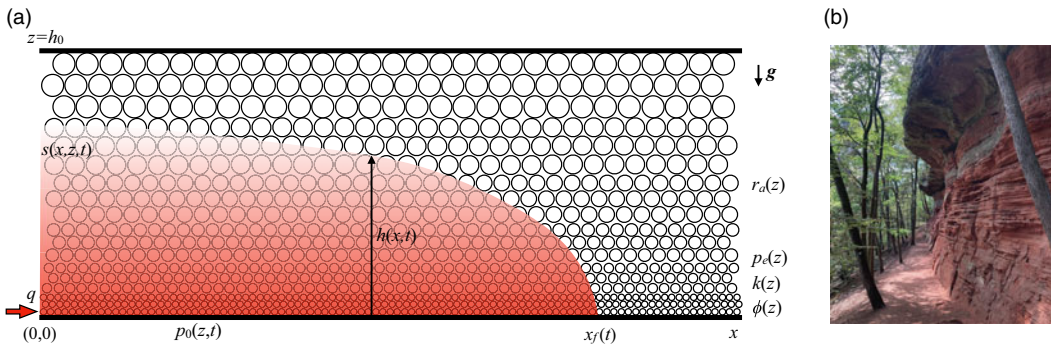


Figure 1. (a) Sketch of an unsaturated current invading into a porous layer with vertical heterogeneity and (b) a natural porous rock with vertical heterogeneity (Image Copyright: D. Geyer). $r_a(z)$, $\phi(z)$ and $k(z)$ denote the pore radius, porosity and intrinsic permeability, respectively, and $p_e(z) \equiv \gamma \cos \theta / r_a(z)$ denotes the capillary entry pressure. The injection rate, effective saturation and outer envelope of the invading fluid are denoted by q , $s(x, z, t)$, and $h(x, t)$, respectively, and the location of the propagating front is denoted by $x_f(t)$. Also, h_0 represents the thickness of the porous layer.

during oil and gas recovery from porous reservoirs (Saffman & Taylor 1958; Cardoso & Woods 1995; Paterson 1981; Al-Housseiny *et al.* 2012), the propagation, trapping and leakage of CO₂ at geological sequestration sites (Neufeld *et al.* 2009; Gunn & Woods 2011; Pegler *et al.* 2014; Zheng *et al.* 2015a; Hinton & Woods 2018), the drainage, irrigation and migration of groundwater in aquifers (Brooks & Corey 1964; Nordbotten & Celia 2006; Hesse *et al.* 2007; MacMinn *et al.* 2010; Guo *et al.* 2016b), the spreading of pollutants, nutrients and chemicals in soils and sands (Huppert & Woods 1995; Brusseau 1995; Pritchard *et al.* 2001; Golding *et al.* 2011; Hinton & Woods 2019), and the evolution of marine ice sheets, ice shelves and the grounding line (Pegler *et al.* 2013; Kowal & Worster 2015, 2020; Pegler & Worster 2013). Partly inspired by these applications, many fundamental studies have been pursued, for example, to describe the time evolution of the profile shape of the fluid–fluid interface, location of propagating fronts, evolution of fluid saturations and the distribution of pollutant particles. This work also studies the dynamics of gravity current, interfacial and unsaturated flows. Nevertheless, we focus on the influence of wetting and capillary forces, and their interaction with the vertical heterogeneity of a porous layer, which has been overlooked.

Sedimentary porous rocks are often vertically heterogeneous: The porous rocks are typically layered with vertical variations of permeability by orders of magnitude between neighbouring layers, as shown in Figure 1. Within each layer, there exists also modest but (sometimes) non-negligible variations of permeability and porosity (Phillips 1991; Dullien 1992; Huppert & Woods 1995; Zheng *et al.* 2013; Hinton & Woods 2018). For multi-phase flows, capillary pressure can also exhibit significant vertical variations in heterogeneous rocks, e.g. due to the variation of local curvature. Hence, the overall flow behaviours can be altered in both steady and unsteady situations, as can the overall performance in geophysical, environmental and industrial applications. For example, in petroleum and environmental engineering, it has long remained an important research topic to appropriately upscale single- and multi-phase flows in heterogeneous porous layers (Coats *et al.* 1971; Jackson *et al.* 2018). The goal is typically to obtain appropriate relative permeability and capillary pressure curves, which can then be employed in transversely averaged flow and transport models at the reservoir scale (Zheng 2022).

In the context of unsteady flows, to our knowledge, the influence of heterogeneity has been investigated in detail for gravity currents (Huppert & Woods 1995; Zheng *et al.* 2013; Hinton & Woods 2018), imbibition flows (Reyssat *et al.* 2008, 2009), onset of hydrodynamic instabilities (Al-Housseiny *et al.* 2012; Grenfell-Shaw *et al.* 2021), and the transport of tracer and pollutant particles in porous rocks and filtering membranes (Dalwadi *et al.* 2016; Hinton & Woods 2019). A common feature of these flows is that there exists typically a sharp fluid–fluid interface. The current work, nevertheless, looks further

into the overlooked regime of unsteady unsaturated flows, as sketched in Figure 1. Key novel aspects of the current work include the following.

- i. Compared with a previous study on a unified description of gravity current, interfacial and unsaturated flows in homogeneous porous layers (Zheng & Neufeld 2019), the current work further integrates the influence of vertical heterogeneity that could possibly appear in sedimentary porous rocks.
- ii. Compared with a series of previous studies that investigated the time evolution of sharp fluid–fluid interfaces in vertically heterogeneous layers (Hinton & Woods 2018), we further resolve the saturation evolution of both the invading and the ambient fluids.
- iii. Compared with a series of recent studies that model quasi-steady unsaturated flows in porous layers (Golding *et al.* 2011; Zheng 2022), the current work keeps the unsteady term in the governing system and addresses the evolution dynamics of the saturation distribution and interface shape.

This paper is structured as follows. In §2, a theoretical model is first presented on the dynamics of gravity current, interfacial and unsaturated flows in vertically heterogeneous porous layers under the assumption of vertical gravitational-capillary equilibrium. This is followed by example calculations in the Cartesian configuration for some asymptotic and numerical insights. Then, in §3, potential implications of the model and solutions are discussed in the context of geological CO₂ sequestration, considering geophysical and operational parameters. This work is closed in §4 with a brief summary and final remarks on important model assumptions.

2. Theoretical model

We study one-dimensional predominantly horizontal flows in the Cartesian configuration, as illustrated in Figure 1. This set-up mimics some aspects of the displacement process generated from fluid injection through horizontal wells into a layer of sands, soil and rock formation. The injection rate q is assumed to remain constant throughout the entire period of fluid injection. To highlight the influence of vertical heterogeneity, the variation of average pore size is assumed to follow the power-law form of $r_a(z) \sim r_1 z^\delta$, as is the intrinsic permeability $k(z) = k_0(r_1 z^\delta)^2$ and porosity $\phi(z) = \phi_0(r_1 z^\delta)^{2/n}$. Such an assumption on heterogeneity in a model problem, including the correlation between porosity and intrinsic permeability, is consistent with a series of earlier reports (Huppert & Woods 1995; Reyssat *et al.* 2008; Zheng *et al.* 2013; Ciriello *et al.* 2013; Zheng *et al.* 2014; Longo *et al.* 2015; Hinton & Woods 2018; Grenfell-Shaw *et al.* 2021).

Meanwhile, we use the power-law form of relative permeability curves $k_{rn}(s) = k_{rn0} s^\alpha$ and $k_{rw}(s) = (1-s)^\beta$ (Brooks & Corey 1964), where we set $\alpha = \beta = 2$. The capillary pressure curve is also assumed to follow the power-law form of $p_c(s) = \gamma \cos \theta r_a^{-1} (1-s)^{-1/\Lambda}$, with representative values of Λ being $\Lambda = \{1/2, 1, 2, 10\}$. Note that $\Lambda \rightarrow \infty$ suggests the existence of a sharp interface between the invading and the ambient fluids, which is also practically relevant. Note also that the capillary entry pressure follows $p_e(z) = \gamma \cos \theta / (r_1 z^\delta)$ accordingly. The assumptions on the form of the $k_{rn}(s)$, $k_{rw}(s)$ and $p_c(s)$ curves are consistent with a series of earlier studies of unsaturated flows based on experimental observations of CO₂ flooding in Ellerslie sandstone (Golding *et al.* 2011, 2013; Zheng & Neufeld 2019; Zheng 2022).

A major advantage of using the power-law form of vertical heterogeneity is that it leads to an explicit expression for the saturation distribution $s(x, z, t)$ as a function of the profile shape $h(x, t)$. The remaining problem is then to solve for the interface shape evolution $h(x, t)$, which becomes somewhat standard in the context of gravity current flows (Huppert & Woods 1995; Pegler *et al.* 2014; Zheng *et al.* 2015a). Before we move on with detailed calculations, we note that the theory, in principle, applies to any form of vertical heterogeneity (though explicit solutions may not be available), providing that the assumption of vertical gravitational-capillary equilibrium continues to apply.

2.1. Vertical gravitational-capillary equilibrium

When a current is long and thin, the incompressible flow condition ($\nabla \cdot \mathbf{u} = 0$) indicates that the vertical component of the Darcy velocity is negligible, compared with the horizontal component. This is a key feature of the propagation and displacement processes in this work, and is assumed to apply within the entire domain and throughout the entire time evolution. Effectively, the flow is predominantly one-dimensional, as the gravitational and capillary forces balance each other in the vertical direction (Golding *et al.* 2011; Zheng & Neufeld 2019). Correspondingly, the pressure distribution within the invading and displaced fluids $p_n(x, z, t)$ and $p_w(x, z, t)$ follows

$$\frac{\partial p_n}{\partial z} = -\rho_n g, \quad \text{and} \quad \frac{\partial p_w}{\partial z} = -\rho_w g, \tag{1a,b}$$

which can be combined to provide a relationship between the capillary pressure $p_c(x, z, t) = p_n(x, z, t) - p_w(x, z, t)$ and buoyancy $\Delta\rho g$ as

$$\frac{\partial p_c}{\partial z} = -\Delta\rho g. \tag{2}$$

This is an important result, which leads to an explicit expression between the saturation distribution $s(x, z, t)$ and the interface shape $h(x, t)$ as we show next.

By integrating (2) along the z direction, we next obtain

$$p_c(s, z) - p_e(z) = -\Delta\rho g[z - h(x, t)]. \tag{3}$$

The boundary conditions employed upon integration are that $s[x, z = h(x, t), t] = 0$ for the effective saturation and $p_c(s = 0, z) \equiv p_e(z)$ for the capillary pressure along the outer envelope of the invading non-wetting fluid $z = h(x, t)$. Equation (3) can then be combined with $p_c(s, z) = \frac{\gamma \cos \theta}{r_a(z)}(1 - s)^{-1/\Lambda}$ to provide an explicit expression for the effective saturation $s(x, z, t)$ as

$$s(x, z, t) = 1 - \left(1 - \frac{\Delta\rho g[z - h(x, t)] r_a(z)}{\gamma \cos \theta} \right)^{-\Lambda}, \tag{4}$$

where we have assumed that the contact angle θ remains constant. Here, Λ is a fitting parameter, representing the pore-size distribution. Smaller Λ corresponds to a wider distribution of pore size, while $\Lambda \rightarrow +\infty$ indicates the limit of monodisperse pores with the same radius r_a . Representative values for Λ that have been employed in previous studies are $\Lambda = \{1/2, 1, 2, 10\}$ for the application of geological CO₂ sequestration (Golding *et al.* 2011, 2013; Zheng & Neufeld 2019; Zheng 2022). With (4), we know immediately that once $h(x, t)$ is obtained, the saturation field $s(x, z, t)$ can be obtained conveniently.

In addition, under the assumption of vertical gravitational-capillary equilibrium, we can obtain the pressure distribution $p(x, z, t)$ by integrating (1) vertically:

$$p_n(x, z, t) = p_0(x, t) - \rho_n g z \quad \text{for } 0 \leq z \leq h(x, t), \tag{5a}$$

$$p_w(x, z, t) = p_0(x, t) - \rho_n g h - \rho_w g(z - h) - p_e(z) \quad \text{for } 0 \leq z \leq h_0, \tag{5b}$$

where $p_0(x, t)$ is a reference pressure of the invading non-wetting fluid along the horizontal boundary ($z = 0$). The pressure gradient along the horizontal direction can then be calculated as

$$\frac{\partial p_n}{\partial x}(x, t) = \frac{\partial p_0}{\partial x}(x, t) \quad \text{for } 0 \leq z \leq h(x, t), \tag{6a}$$

$$\frac{\partial p_w}{\partial x}(x, t) = \frac{\partial p_0}{\partial x}(x, t) + \Delta\rho g \frac{\partial h}{\partial x}(x, t) \quad \text{for } 0 \leq z \leq h_0, \tag{6b}$$

which can be substituted back into the generalised Darcy’s law to provide the horizontal velocities of each phase. It is of interest to note that neither $\partial p_n / \partial x$ nor $\partial p_w / \partial x$ varies along the vertical direction z , but in contrast, the pressure distribution $p_n(x, z, t)$ and $p_w(x, z, t)$ both exhibit vertical variations. This is a common feature of flow under vertical equilibrium.

2.2. Evolution equation

Following standard derivations (Zheng & Neufeld 2019), it is convenient to show that the time evolution of the interface shape $h(x, t)$ and saturation distribution $s(x, z, t)$ is governed by the following set of differential and integral equations:

$$(1 - S_r) \frac{\partial I_s(h)}{\partial t} + q \frac{\partial}{\partial x} \left[\frac{MI_n(h)}{MI_n(h) + I_w(h)} \right] - \frac{\Delta \rho g}{\mu_n} \frac{\partial}{\partial x} \left[\frac{I_n(h)I_w(h)}{MI_n(h) + I_w(h)} \frac{\partial h}{\partial x} \right] = 0, \tag{7a}$$

$$I_s(h) \equiv \int_0^{h(x,t)} \phi_0(r_1 z^\delta)^{2/n} s(x, z, t) dz, \tag{7b}$$

$$I_n(h) \equiv \int_0^{h(x,t)} k_0(r_1 z^\delta)^2 k_{rn}(s) dz, \quad I_w(h) \equiv \int_0^{h_0} k_0(r_1 z^\delta)^2 k_{rw}(s) dz, \tag{7c}$$

and in particular, there is the explicit solution of $s(x, z, t)$ as a function of $h(x, t)$:

$$s(x, z, t) = 1 - \left(1 - \frac{\Delta \rho g [z - h(x, t)] r_1 z^\delta}{\gamma \cos \theta} \right)^{-\Lambda}, \tag{8}$$

where we now substituted in the power-law form of $r_a(z) \sim r_1 z^\delta$. As mentioned before, these results are based on the key assumption of vertical gravitational-capillary equilibrium for predominantly one-dimensional flows.

The initial-boundary value problem (7a) for $h(x, t)$ can be solved, providing appropriate initial and boundary conditions. When a fluid is injected at a constant rate q into a porous layer initially saturated with another immiscible fluid, the initial and boundary conditions are

$$h(x, 0) = 0, \tag{9a}$$

$$h(x_f(t), t) = 0, \tag{9b}$$

$$\left[\frac{qMI_n(h)}{MI_n(h) + I_w(h)} - \frac{\Delta \rho g}{\mu_n} \frac{I_n(h)I_w(h)}{MI_n(h) + I_w(h)} \frac{\partial h}{\partial x} \right] \Big|_{x=0} = q. \tag{9c}$$

Physically, (9a) represents an initial environment filled entirely with the ambient fluid within the entire domain. Equation (9b) is a frontal condition, with $x_f(t)$ denoting the location of a propagating front along the bottom boundary. Equation (9c) is a flux condition at the origin $x = 0$ and is obtained by integrating (7a) from $x = 0$ (location of fluid injection) towards $x = x_f(t)$ (location of the propagating front), applying the integral constraint of global mass conservation:

$$(1 - S_r) \int_0^{x_f(t)} I_s(h) dx = qt. \tag{10}$$

To obtain the flux boundary condition (9c), it is also assumed that there is no fluid entrainment at the location of the front at $x = x_f(t)$, such that the local flux is zero at $x = x_f(t)$. Similar treatment has been employed previously in a series of fluid injection problems (Zheng *et al.* 2015a). The problem formulation (7), (8) and (9), in principle, works for any functional form of $k_{rn}(s)$ and $k_{rw}(s)$, and here we impose $k_{rn}(s) = k_{rn0} s^\alpha$ and $k_{rw}(s) = (1 - s)^\beta$ for the example calculations, as summarised in Table 1.

2.3. Non-dimensionalisation

We next non-dimensionalise (7), (8) and (9), and then discuss the asymptotic and numerical solutions and their physical interpretations. The dimensionless length, height, thickness and time are denoted by $\bar{x} \equiv x/x_c$, $\bar{z} \equiv z/h_0$, $\bar{h} \equiv h/h_0$ and $\bar{t} \equiv t/t_c$, where the characteristic length and time scales are chosen as

$$x_c = \frac{\Delta \rho g k_0 k_{rn0} r_1^2 h_0^{2\delta+2}}{\mu_n q} \quad \text{and} \quad t_c = \frac{(1 - S_r) \Delta \rho g k_0 k_{rn0} \phi_0 r_1^{2/n+2} h_0^{2\delta/n+2\delta+3}}{\mu_n q^2}. \tag{11a,b}$$

Table 1. Definition and physical meaning of the seven dimensionless parameters α , β , Λ , δ , n , N and B for predominantly one-dimensional flows in vertically heterogeneous porous layers

Parameter	Definition	Physical description
α	$k_{rn}(s) = k_{rn0} s^\alpha$	nonlinearity of relative permeability $k_{rn}(s)$
β	$k_{rw}(s) = (1 - s)^\beta$	nonlinearity of relative permeability $k_{rw}(s)$
Λ	$p_c/p_e = (1 - s)^{-1/\Lambda}$	nonlinearity of capillary pressure $p_c/p_e \equiv f(s)$
δ	$r_a(z) = r_1 z^\delta$	nonlinearity of average pore size distribution $r_a(z)$
n	$k(\phi) = k_n \phi^n$	connection between intrinsic permeability and porosity
N	$k_{rn0} \mu_w / \mu_n$	modified viscosity ratio
B	$\Delta \rho g r_1 h_0^{\delta+1} / \gamma \cos \theta$	competition between gravitational and capillary forces

The scales x_c and t_c are chosen such that the unsteady, advective and diffusive terms balance each other in (7a) at $t \approx t_c$ for modest values of M . The dimensionless frontal locations are $\bar{x}_f(\bar{t}) \equiv x_f(t)/x_c$, and the dimensionless version of (7) and (8) becomes

$$\frac{\partial \bar{I}_s(\bar{h})}{\partial \bar{t}} + \frac{\partial}{\partial \bar{x}} \left[\frac{N \bar{I}_n(\bar{h})}{N \bar{I}_n(\bar{h}) + \bar{I}_w(\bar{h})} \right] - \frac{\partial}{\partial \bar{x}} \left[\frac{\bar{I}_n(\bar{h}) \bar{I}_w(\bar{h})}{N \bar{I}_n(\bar{h}) + \bar{I}_w(\bar{h})} \frac{\partial \bar{h}}{\partial \bar{x}} \right] = 0, \tag{12a}$$

$$\bar{I}_s(\bar{h}) \equiv \int_0^{\bar{h}(\bar{x}, \bar{t})} \bar{z}^{2\delta/n} s(\bar{x}, \bar{z}, \bar{t}) d\bar{z}, \tag{12b}$$

$$\bar{I}_n(\bar{h}) \equiv \int_0^{\bar{h}(\bar{x}, \bar{t})} \bar{z}^{2\delta} s^\alpha d\bar{z}, \quad \bar{I}_w(\bar{h}) \equiv \int_0^{\bar{h}(\bar{x}, \bar{t})} \bar{z}^{2\delta} (1 - s)^\beta d\bar{z} + \frac{1 - \bar{h}^{2\delta+1}}{2\delta + 1} \tag{12c}$$

and

$$s(\bar{x}, \bar{z}, \bar{t}) = 1 - \left(1 - B [\bar{z} - \bar{h}(\bar{x}, \bar{t})] \bar{z}^\delta \right)^{-\Lambda}, \tag{13}$$

where the vertical integrals $\bar{I}_s(\bar{h})$, $\bar{I}_n(\bar{h})$ and $\bar{I}_w(\bar{h})$ are made dimensionless based on

$$\bar{I}_s(\bar{h}) \equiv \frac{I_s(h)}{\phi_0 r_1^{2/n} h_0^{2\delta/n+1}}, \quad \bar{I}_n(\bar{h}) \equiv \frac{I_n(h)}{k_0 k_{rn0} r_1^2 h_0^{2\delta+1}} \quad \text{and} \quad \bar{I}_w(\bar{h}) \equiv \frac{I_w(h)}{k_0 r_1^2 h_0^{2\delta+1}}. \tag{14a,b,c}$$

We have introduced two dimensionless parameters N and B in (12a) and (13), defined as

$$N \equiv k_{rn0} M = k_{rn0} \frac{\mu_w}{\mu_n} \quad \text{and} \quad B \equiv \frac{\Delta \rho g r_1 h_0^{\delta+1}}{\gamma \cos \theta}. \tag{15a,b}$$

Physically, N represents a ‘modified’ viscosity ratio, now including the influence of the end-point relative permeability k_{rn0} of the invading fluid. This is also recognised by Zheng & Neufeld (2019) for predominantly one-dimensional flows in an homogeneous porous layer. The Bond number B provides a measurement of the competition between the gravitational and capillary forces across the entire thickness of a vertically heterogeneous porous layer. Note also that B reduces to $1/H_e$ for Zheng & Neufeld (2019) for flow in homogeneous layers, where H_e is effectively a dimensionless capillary entry length. Similarly, $1/B$ can also be understood as a dimensionless capillary entry length in a vertically heterogeneous layer. The solutions are under the influence of seven dimensionless parameters α , β , Λ , δ , n , N and B , the definition and physical meaning of which are summarised in Table 1.

Meanwhile, the initial and boundary conditions (9) can also be made dimensionless as

$$\bar{h}(\bar{x}, 0) = 0, \tag{16a}$$

$$\bar{h}(\bar{x}_f(\bar{t}), \bar{t}) = 0, \tag{16b}$$

$$\left[\frac{N \bar{I}_n(\bar{h})}{N \bar{I}_n(\bar{h}) + \bar{I}_w(\bar{h})} - \frac{\bar{I}_n(\bar{h}) \bar{I}_w(\bar{h})}{N \bar{I}_n(\bar{h}) + \bar{I}_w(\bar{h})} \frac{\partial \bar{h}}{\partial \bar{x}} \right] \Big|_{\bar{x}=0} = 1. \tag{16c}$$

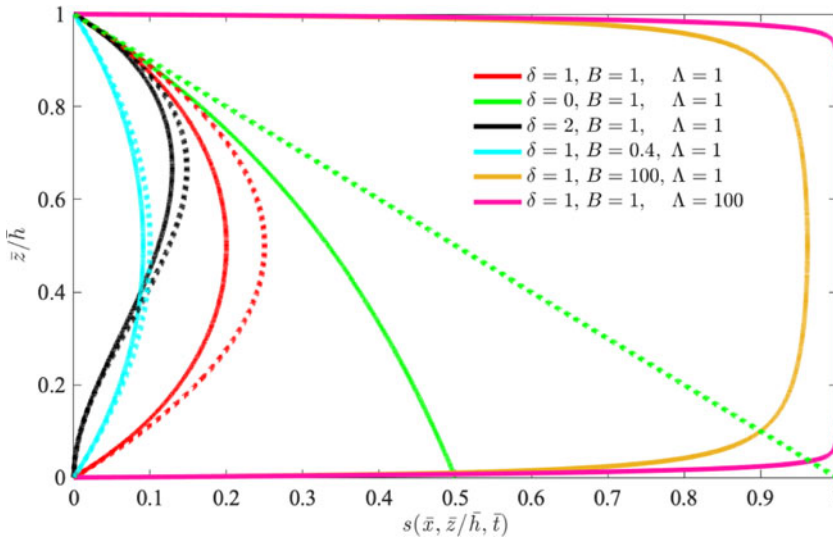


Figure 2. Representative solutions for the saturation field $s(\bar{x}, \bar{z}/\bar{h}, \bar{t})$ along the vertical direction $\bar{z}/\bar{h}(\bar{x}, \bar{t})$ at any horizontal location \bar{x} at any time \bar{t} . The solid curves are based on (13), while the dashed curves are the asymptotes (17) that apply only when $B \ll 1$ for significantly unsaturated flows. The saturation field approaches the sharp-interface solution (35) when $B \gg 1$ or when $\Lambda \gg 1$.

We are now ready to explore solutions of the dimensionless system (12) subject to (16). In particular, (13) indicates that the saturation field $s(\bar{x}, \bar{z}, \bar{t})$ is under the influence of three dimensionless control parameters: δ , a description of vertical heterogeneity; Λ , an indication of the pore size distribution; and B , a measurement of the competition between buoyancy and capillary forces. Typical solutions of $s(\bar{x}, \bar{z}, \bar{t})$ are shown in Figure 2 for representative values of δ , B and Λ of practical relevance. We observe that $s(\bar{x}, \bar{z}, \bar{t})$ is not monotonic along the z direction when $\delta > 0$, which indicates there exists no flow of the invading fluid along $z = 0$ and is consistent with the assumption that $k = 0$ and $\phi = 0$ along $z = 0$.

2.4. Significantly unsaturated and sharp-interface flow regimes

Analytical insights can be obtained in the significantly unsaturated and sharp-interface flow regimes, as we now discuss in §§ 2.4.1 and 2.4.2, respectively. Particular focus is placed on the unsaturated flow regime in the present work, since the key features in the sharp-interface flow regime have already been discussed (Huppert & Woods 1995; Hinton & Woods 2018). Due to the page limit for the maintext, we only show the early-time and late-time asymptotic behaviours in § 2.4.1, and in the supplementary material (SM) available at <http://dx.doi.org/10.1017/flo.2025.13>, we include also numerical solutions to demonstrate the time transition across time scales and how the flow approaches the early-time unconfined and late-time confined asymptotes in the corresponding asymptotic limits. The numerical scheme employed is also briefly described in the SM.

2.4.1. Significantly unsaturated flow regime

For modest values of B , the fluid saturation $s(\bar{x}, \bar{z}, \bar{t})$ exhibits spatial variations due to the influence of the wetting and capillary forces. When $B \ll 1$, named as the significantly unsaturated flow regime, (13) can be expanded as

$$s(\bar{x}, \bar{z}, \bar{t}) = \begin{cases} B\Lambda [\bar{h}(\bar{x}, \bar{t}) - \bar{z}] \bar{z}^\delta + O(B^2), & 0 \leq \bar{z} \leq \bar{h}(\bar{x}, \bar{t}), \\ 0, & \bar{h}(\bar{x}, \bar{t}) < \bar{z} \leq 1, \end{cases} \quad (17)$$

as a leading-order approximate for the saturation field. Equation (17) is plausible, since it allows analytical insights to understand the influence of vertical heterogeneity on unsaturated flows in porous layers. Based on (17), the rescaled solution $s(\bar{x}, \bar{z}, \bar{t})/B\Lambda$ is only under the influence of δ , the nonlinearity exponent for the pore size distribution $r_a(z) = r_1 z^\delta$ of the porous layer. Equation (17) is also included in Figure 2 as the dashed curves, which is to be compared with the original solution (13).

To start, by substituting (17) back into (12b,c), we obtain approximate solutions for the vertical integrals $\bar{I}_s(\bar{h})$, $\bar{I}_n(\bar{h})$ and $\bar{I}_w(\bar{h})$ within the significantly unsaturated flow regime ($B \ll 1$):

$$\bar{I}_s(\bar{h}) \sim \frac{B\Lambda \bar{h}^{2\delta/n+\delta+2}}{(2\delta/n + \delta + 1)(2\delta/n + \delta + 2)}, \tag{18a}$$

$$\bar{I}_n(\bar{h}) \sim \frac{2B^2\Lambda^2 \bar{h}^{4\delta+3}}{(4\delta + 1)(4\delta + 2)(4\delta + 3)}, \tag{18b}$$

$$\bar{I}_w(\bar{h}) \sim \frac{1}{2\delta + 1} - \frac{2B\Lambda \bar{h}^{3\delta+2}}{(3\delta + 1)(3\delta + 2)} + \frac{2B^2\Lambda^2 \bar{h}^{4\delta+3}}{(4\delta + 1)(4\delta + 2)(4\delta + 3)}, \tag{18c}$$

where we have further imposed $\alpha = \beta = 2$ for the relative permeability curves Golding *et al.* 2011; Zheng & Neufeld 2019).

(i) *Early-time asymptotic solutions* ($\bar{t} \ll 1$)

At early times, defined by $\bar{t} \ll 1$, the front of the invading fluid locates at $\bar{x}_f(\bar{t}) \ll 1$ and the thickness of the invading fluid is also small $\bar{h}(\bar{x}, \bar{t}) \ll 1$ such that $\bar{I}_n(\bar{h}) \ll \bar{I}_w(\bar{h})$. In this case, the nonlinear diffusive term is much greater than the advective term, and the governing system (12a) further reduces to

$$\frac{\partial \bar{I}_s(\bar{h})}{\partial \bar{t}} - \frac{\partial}{\partial \bar{x}} \left[\bar{I}_n(\bar{h}) \frac{\partial \bar{h}}{\partial \bar{x}} \right] = 0. \tag{19}$$

Then, by substituting (18) into (19), we arrive at a nonlinear diffusion equation for the time evolution of the interface shape $\bar{h}(\bar{x}, \bar{t})$ that is very similar to those obtained by Boussinesq (1904) and Huppert (1982):

$$\frac{\partial \bar{h}^{2\delta/n+\delta+2}}{\partial \bar{t}} - A_1 \frac{\partial}{\partial \bar{x}} \left(\bar{h}^{4\delta+3} \frac{\partial \bar{h}}{\partial \bar{x}} \right) = 0, \quad \text{where } A_1 \equiv \frac{2B\Lambda(2\delta/n + \delta + 1)(2\delta/n + \delta + 2)}{(4\delta + 1)(4\delta + 2)(4\delta + 3)}. \tag{20}$$

The partial differential equation (PDE) (20) can be solved, providing a frontal condition $\bar{h}(\bar{x}_f(\bar{t}), \bar{t}) = 0$ and an integral condition for the fluid volume:

$$\int_0^{\bar{x}_f(\bar{t})} A_2 \bar{h}^{2\delta/n+\delta+2} d\bar{x} = \bar{t}, \quad \text{where } A_2 \equiv \frac{B\Lambda}{(2\delta/n + \delta + 1)(2\delta/n + \delta + 2)}. \tag{21}$$

Nevertheless, it is important to note that, physically, (20) and (21) describe the invasion of a capillary film into a porous layer, rather than the propagation of a viscous gravity current (Huppert 1982). This is more clearly seen in the dimensional form of (20), which depends explicitly on surface tension γ rather than buoyancy $\Delta\rho g$. The interface shape $\bar{h}(\bar{x}, \bar{t})$ is now under the influence of three dimensionless parameters: δ and n , which characterise the intrinsic properties of the porous layer, and $B\Lambda$, an indication of the competition between buoyancy and capillary forces in an heterogeneous environment. Also, there is no role of the modified viscosity ratio N , since flow of the invading fluid is unconfined and flow of the displaced fluid is negligible. Once $\bar{h}(\bar{x}, \bar{t})$ is obtained from solving (20) and (21), the saturation field $s(\bar{x}, \bar{z}, \bar{t})$ can then be obtained from (17).

Self-similar solutions can also be explored for the time evolution of the interface shape $\bar{h}(\bar{x}, \bar{t})$, as is suggested by the form of (20) and (21). We can start by defining a similarity transform as

$$\xi \equiv \frac{\bar{x}}{\xi_f A_1^{2\delta/n+\delta+2} A_2^{2\delta/n-3\delta-2} \bar{t}^{4\delta+4/2\delta/n+5\delta+6}}, \tag{22a}$$

$$\bar{h}(\bar{x}, \bar{t}) = \xi_f^{-2} A_1^{-2} A_2^{-1} \bar{t}^{1/2\delta/n+5\delta+6} g(\xi), \tag{22b}$$

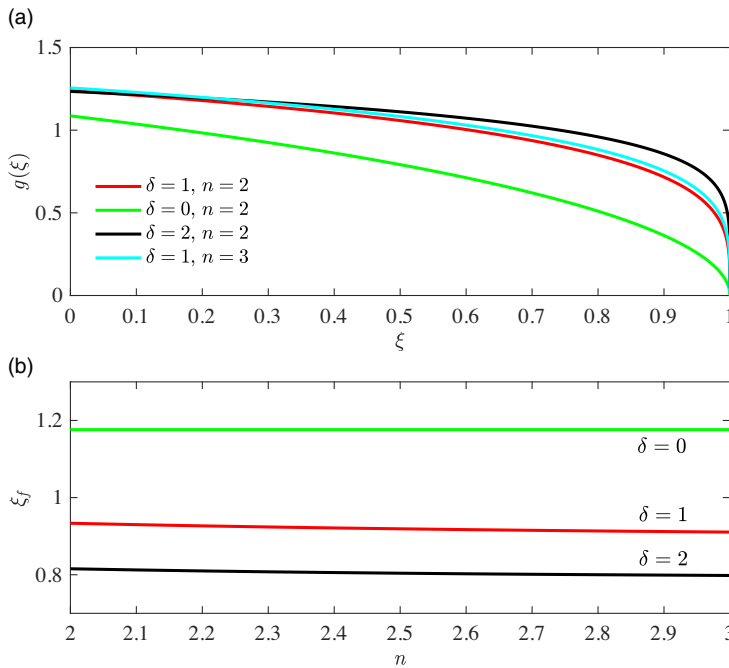


Figure 3. Influence of heterogeneity on (a) the early-time self-similar solution $g(\xi)$ and (b) the frontal location ξ_f for selected values of δ and n from solving (23). The case of $\delta = 0$ is also plotted as a comparison, which represents unconfined unsaturated flow in a homogeneous porous layer.

where $\xi \in [0, 1]$, with the propagating front locating at $\bar{x}_f(\bar{t}) = \xi_f A_1^{\frac{2\delta/n+\delta+2}{2\delta/n+5\delta+6}} A_2^{\frac{2\delta/n-3\delta-2}{2\delta/n+5\delta+6}} t^{\frac{4\delta+4}{2\delta/n+5\delta+6}}$ as time progresses. Under transform (22a,b), (20) and (21) are transformed into

$$\frac{2\delta/n + \delta + 2}{2\delta/n + 5\delta + 6} g^{2\delta/n+\delta+2} - \frac{4\delta + 4}{2\delta/n + 5\delta + 6} \xi \frac{dg^{2\delta/n+\delta+2}}{d\xi} - \frac{d}{d\xi} \left(g^{4\delta+3} \frac{dg}{d\xi} \right) = 0, \tag{23a}$$

$$\xi_f = \left(\int_0^1 g^{2\delta/n+\delta+2} d\xi \right)^{\frac{2\delta/n-3\delta-2}{2\delta/n+5\delta+6}}, \tag{23b}$$

for the self-similar interface shape $g(\xi)$ and frontal location ξ_f . The above transform and descriptions from (20) to (23) are analogous exactly to those that describe the propagation of viscous gravity currents (Huppert 1982). We also note that, while the interface shape $\bar{h}(\bar{x}, \bar{t})$ and frontal location $\bar{x}_f(\bar{t})$ depend on $B\Lambda$, a measurement of the wetting and capillary effects, the self-similar shape $g(\xi)$ and prefactor ξ_f rely only on δ and n that describe the intrinsic properties of a vertical heterogeneity.

The ordinary differential equation (ODE) (23a) can be solved numerically from $\xi = 1 - \lambda$ towards $\xi = 0^+$ with $\lambda \ll 1$. The boundary conditions at $\xi = 1 - \lambda$ are

$$g(1 - \lambda) \sim \left(\frac{2\delta/n + 5\delta + 6}{4\delta + 4} \right)^{\frac{1}{2\delta/n-3\delta-2}} \lambda^{-\frac{1}{2\delta/n-3\delta-2}}, \tag{24a}$$

$$\left. \frac{dg}{d\xi} \right|_{1-\lambda} \sim \left(\frac{2\delta/n + 5\delta + 6}{4\delta + 4} \right)^{\frac{1}{2\delta/n-3\delta-2}} \frac{1}{2\delta/n - 3\delta - 2} \lambda^{-\frac{2\delta/n-3\delta-1}{2\delta/n-3\delta-2}}, \tag{24b}$$

as obtained from a local analysis of (23a) that $g \sim [(2\delta/n + 5\delta + 6)/(4\delta + 4)]^{1/(2\delta/n-3\delta-2)} (1 - \xi)^{-1/(2\delta/n-3\delta-2)}$ as $\xi \rightarrow 1^-$. Once $g(\xi)$ is known, the prefactor ξ_f can also be calculated from (23b), and the dependence on δ and n can also be obtained. Typical results are shown in Figure 3a for the interface

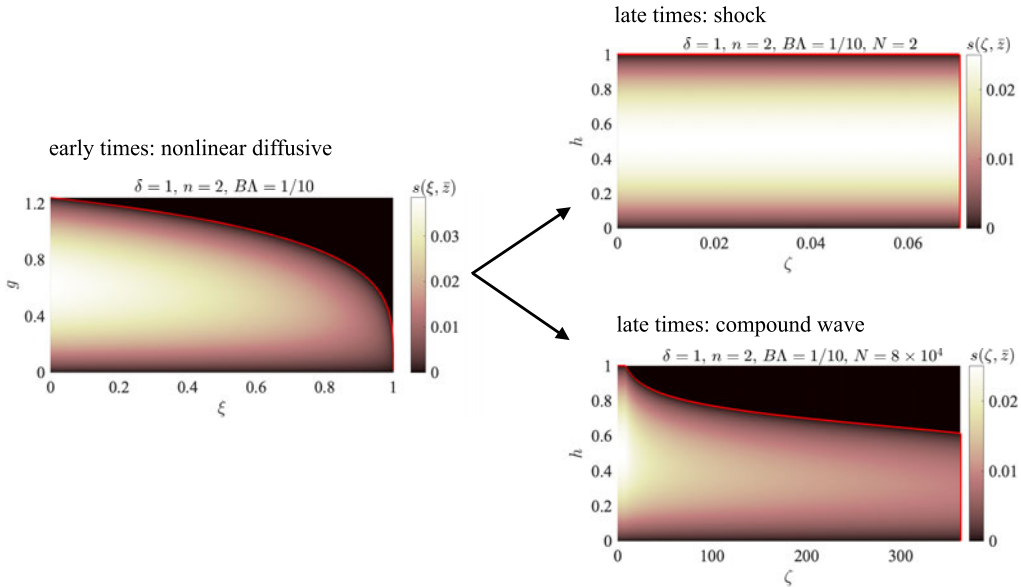


Figure 4. Time evolution of the profile shape $\bar{h}(\bar{x}, \bar{t})$ based on the early- and late-time self-similar solutions (23) and (29) and the saturation distribution $s(\bar{x}, \bar{z}, \bar{t})$ based on (17) in the significantly unsaturated flow regime ($B \ll 1$). $\bar{h}(\bar{x}, \bar{t})$ evolves from a capillary film shape into either a compound-wave shape ($N > N_c$) or a shock shape ($N \leq N_c$), depending on the modified viscosity ratio $N \equiv k_{rn0} \mu_d / \mu_i$. We have imposed $\delta = 1$, $n = 2$ and $B\Lambda = 1/10$ in this example calculation.

shape $g(\xi)$, employing Matlab subroutine ODE45 (or ODE15s) setting $\lambda = 10^{-8}$. The prefactor ξ_f for the frontal location is also shown in Figure 3b for selected values of δ and n . It is found that the dependence of ξ_f on n is rather weak. The saturation distribution $s(\bar{x}, \bar{z}, \bar{t})$, in addition, is shown in Figure 4, based on (17), where we imposed $\{\delta, n, B\Lambda\} = \{1, 2, 1/10\}$ as an example.

It is also of interest to provide a self-consistency check on the time scale for the condition of $\bar{h} \ll 1$ to apply. Based on (22b), we obtain that $\bar{h} \approx (\bar{t}/A_1 A_2^2)^{1/(2\delta/n+5\delta+6)}$, which provides a time scale of $\bar{t}_{c1} \approx A_1 A_2^2$ for the interface to attach at both the top and bottom boundaries, i.e. $\bar{h}(0, \bar{t}_{c1}) \approx 1$. In other words, it is required that $\bar{t} \ll \bar{t}_{c1}$ for the early-time self-similar solution to apply. It is also suggested that the transition time scale $\bar{t}_{c1} \propto (B\Lambda)^3$, which can be significantly impacted by the wetting and capillary effects. In addition, $\bar{t}_{c1} \propto 1/(4\delta + 1)(4\delta + 2)(4\delta + 3)(2\delta/n + \delta + 1)(2\delta/n + \delta + 2)$, so it is also under the influence of vertical heterogeneity.

(ii) Late-time asymptotic solutions ($\bar{t} \gg 1$)

At late times, defined by $\bar{t} \gg 1$, we expect the length of the current $\bar{x}_f(\bar{t}) \gg 1$, as it continues to elongate. Eventually, the contribution of the diffusive term ($\propto \bar{x}_f^{-2}$) becomes much smaller compared with the advective term ($\propto \bar{x}_f^{-1}$) in PDE (12a), except possibly in a narrow boundary layer near the propagating front $\bar{x}_f(\bar{t})$, where singular perturbation effects become important. In the present work, we neglect such a frontal region and explore the late-time asymptotic behaviours of $\bar{h}(\bar{x}, \bar{t})$ simply by studying the advective equation

$$\frac{\partial \bar{I}_s(\bar{h})}{\partial \bar{t}} + \frac{\partial}{\partial \bar{x}} \left[\frac{N \bar{I}_n(\bar{h})}{N \bar{I}_n(\bar{h}) + \bar{I}_w(\bar{h})} \right] = 0. \tag{25}$$

Self-similar solutions can also be explored, now by defining a similarity variable as $\zeta \equiv \bar{x}/\bar{t}$, and hence $\bar{h}(\bar{x}, \bar{t}) = h(\zeta)$. The PDE (25) is then transformed into

$$-\zeta \frac{d\bar{I}_s(\bar{h})}{d\zeta} + \frac{d}{d\zeta} \left[\frac{N\bar{I}_n(\bar{h})}{N\bar{I}_n(\bar{h}) + \bar{I}_w(\bar{h})} \right] = 0, \tag{26}$$

the solution of which is under the influence of all seven dimensionless control parameters $\alpha, \beta, \Lambda, \delta, n, N$ and B . Neglecting the solution branch of $d\bar{h}/d\zeta = 0$, ODE (26) can be further rearranged to provide an algebraic equation for the self-similar solution $\bar{h}(\zeta)$ as

$$\zeta = \frac{d}{d\bar{h}} \left[\frac{N\bar{I}_n(\bar{h})}{N\bar{I}_n(\bar{h}) + \bar{I}_w(\bar{h})} \right] \bigg/ \frac{d\bar{I}_s(\bar{h})}{d\bar{h}}. \tag{27}$$

Once $\bar{h}(\zeta)$ is known, the saturation field $s(\zeta, \bar{z})$ can also be calculated based on (17).

Again, we look into the significantly unsaturated flow regime ($B \ll 1$), when the integrals $\bar{I}_s(\bar{h})$, $\bar{I}_n(\bar{h})$ and $\bar{I}_w(\bar{h})$ can be approximated by (18). Then, by substituting (18) into (25), we obtain

$$\frac{\partial \bar{h}^{2\delta/n+\delta+2}}{\partial \bar{t}} + \frac{\partial}{\partial \bar{x}} \left[\frac{C_1 N \bar{h}^{4\delta+3}}{1 - C_2 \bar{h}^{3\delta+2} + C_3 (N+1) \bar{h}^{4\delta+3}} \right] = 0, \tag{28a}$$

$$\text{with } C_1 \equiv \frac{2B\Lambda(2\delta+1)(2\delta/n+\delta+1)(2\delta/n+\delta+2)}{(4\delta+1)(4\delta+2)(4\delta+3)}, \tag{28b}$$

$$C_2 \equiv \frac{2B\Lambda(2\delta+1)}{(3\delta+1)(3\delta+2)}, \quad C_3 \equiv \frac{2B^2\Lambda^2(2\delta+1)}{(4\delta+1)(4\delta+2)(4\delta+3)}, \tag{28c}$$

for the time evolution of $\bar{h}(\bar{x}, \bar{t})$, or

$$\zeta = \frac{1}{(2\delta/n+\delta+2) \bar{h}^{2\delta/n+\delta+1}} \frac{d}{d\bar{h}} \left[\frac{C_1 N \bar{h}^{4\delta+3}}{1 - C_2 \bar{h}^{3\delta+2} + C_3 (N+1) \bar{h}^{4\delta+3}} \right] \tag{29a}$$

$$= \frac{(4\delta+3)C_1 N \bar{h}^{-2\delta/n+3\delta+1} - (\delta+1)C_1 C_2 N \bar{h}^{-2\delta/n+6\delta+3}}{(2\delta/n+\delta+2)[1 - C_2 \bar{h}^{3\delta+2} + C_3 (N+1) \bar{h}^{4\delta+3}]^2}, \tag{29b}$$

for a self-similar solution $\bar{h}(\zeta)$ at late times. Solutions to (28) or (29) are under the influence of four dimensionless parameters: δ, n, N and $B\Lambda$, and once again, B and Λ function together as a group $B\Lambda$.

To explore the solution structure of the advective system, we first comment on the height of the current \bar{h}_i at the inlet $\bar{x} = 0$. By substituting (18) into (16c) and neglecting the diffusive term that is $\propto \partial \bar{h} / \partial \bar{x}$ in (16c), it is shown that the inlet height \bar{h}_i must satisfy $\bar{I}_w(\bar{h}_i) = 0$, i.e.

$$\frac{1}{2\delta+1} - \frac{2B\Lambda \bar{h}_i^{3\delta+2}}{(3\delta+1)(3\delta+2)} + \frac{2B^2\Lambda^2 \bar{h}_i^{4\delta+3}}{(4\delta+1)(4\delta+2)(4\delta+3)} = 0, \tag{30}$$

in the significantly unsaturated regime ($B \ll 1$). However, when $\delta > 0$ and $B\Lambda > 0$, there is no solution for (30) for $\bar{h}_i \in (0, 1)$. Therefore, the inlet height must always be $\bar{h}_i = 1$ at late times, with $|\partial \bar{h} / \partial \bar{x}|(0, t) > 0$ to satisfy boundary condition (16c). This conclusion is also consistent with the numerical observations when we solve PDE (12a).

Correspondingly, when $\delta > 0$, (29) leads to two solution branches in the significantly unsaturated flow regime ($B \ll 1$): (i) compound-wave solutions for sufficiently large viscosity contrast $N > N_c$; and (ii) shock solutions for $N \leq N_c$, where N_c is a critical viscosity ratio that depends on the value of δ, n and $B\Lambda$. To obtain the compound-wave solutions, a shock front of height $\bar{h}_s \in (0, 1)$ is inserted at an appropriate location ζ_s to ensure the conservation of total fluid volume. Based on (18a), the total volume of the invading fluid $d\bar{I}_s(\bar{h})$ within a thin layer $[\bar{h}, \bar{h} + d\bar{h}]$ is given by

$$d\bar{I}_s(\bar{h}) = \frac{B\Lambda \bar{h}^{2\delta/n+\delta+1}}{(2\delta/n+\delta+1)} d\bar{h}, \tag{31}$$

which leads to

$$\int_0^{\bar{h}_s} \zeta(\bar{h}) \bar{h}^{2\delta/n+\delta+1} d\bar{h} = \zeta_s \int_0^{\bar{h}_s} \bar{h}^{2\delta/n+\delta+1} d\bar{h}, \tag{32}$$

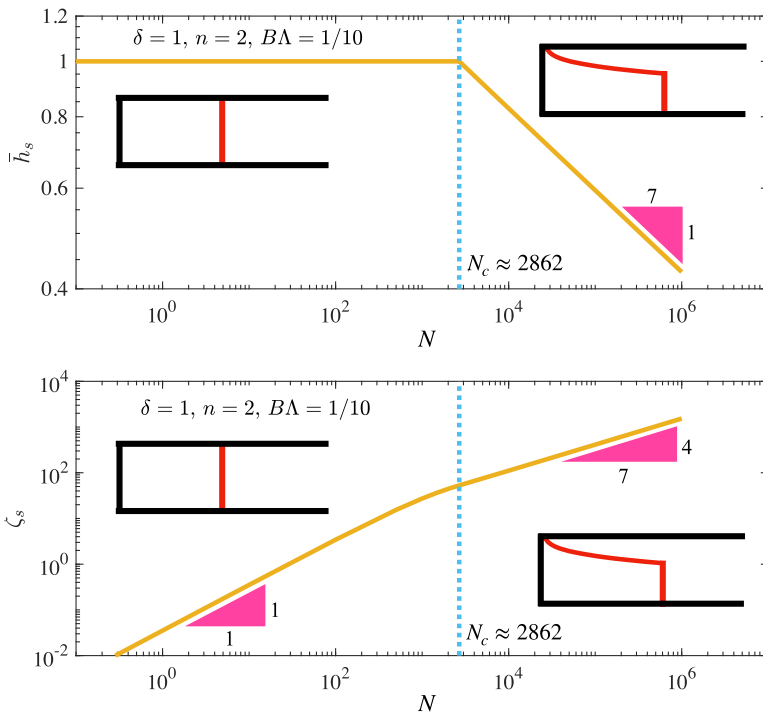


Figure 5. Regime diagram for significantly unsaturated flows in vertically heterogeneous porous layers when the modified viscosity ratio N varies, imposing $\{\delta, n, B\Lambda\} = \{1, 2, 1/10\}$ as an example. The height \bar{h}_s and location $\bar{\zeta}_s$ for the inserted shock front are also shown.

for the height \bar{h}_s and location $\bar{\zeta}_s$ of the inserted shock front. Combining (29) and (32), we can calculate $(\bar{\zeta}_s, \bar{h}_s)$ for any set of $\{\delta, n, N, B\Lambda\}$, bounded by $\bar{h}_s \in (0, 1)$. For shock solutions, we impose $\bar{h}_s = 1$ instead and calculate the frontal location $\bar{\zeta}_s$ based on (32). For example, when we impose $\{\delta, n, N, B\Lambda\} = \{1, 2, 2, 10^{-1}\}$, we obtain a shock with $(\bar{\zeta}_s, \bar{h}_s) \approx (0.0706, 1)$, and when we impose $\{\delta, n, N, B\Lambda\} = \{1, 2, 8 \times 10^4, 1/10\}$, we obtain a compound-wave with $(\bar{\zeta}_s, \bar{h}_s) \approx (363, 0.614)$. The self-similar solutions $\bar{h}(\bar{\zeta})$ in these two cases are also shown in Figure 4 as the red curves, together with the saturation distribution $s(\bar{\zeta}, \bar{z})$, obtained based on (17). It could be of interest to note that compound-wave solutions often appear in the Buckley–Leverett equation for unsaturated flow in porous layers (Buckley & Leverett 1942). They also appear in sharp-interface flows in inclined circular pipes (Seon *et al.* 2007) and horizontal channels (Zheng *et al.* 2015b) upon fluid injection.

Typical solutions of algebraic equations (29) and (32) are also included in Figure 5, which leads to a regime diagram that allocates the compound-wave and shock solutions for different values of the modified viscosity ratio N . A critical viscosity contrast $N_c \approx 2862$ is observed and marked by the dashed lines in Figure 5a,b, when we impose $\{\delta = 1, n = 2, B\Lambda = 10^{-1}\}$ in this example calculation. The height \bar{h}_s and location $\bar{\zeta}_s$ of the inserted shock fronts are also shown in Figures 5a and 5b, respectively. It is also observed that $\bar{h}_s \propto N^{-1/7}$ and $\bar{\zeta}_s \propto N^{4/7}$ for the compound-wave solutions at sufficiently large N , while for the shock solutions ($\bar{h}_s = 1$), the calculations indicate that $\bar{\zeta}_s \propto N$ for smaller N . The scaling behaviours can be explained based on the form of (29): for compound-wave solutions, when we set $\bar{h} = \bar{h}_s \in (0, 1)$ in (29b), for $N \gg 1$, the leading-order balance in the denominator of (29b) then leads to $\bar{h}_s \propto N^{-1/7}$, which then indicates that $\bar{\zeta}_s \propto N\bar{h}_s^3 \propto N^{4/7}$; for shock solutions, imposing $\bar{h}_s = 1$ in (29b), we immediately obtain $\bar{\zeta}_s \propto N$ for $N \ll 1$.

(iii) Time transition between early-time and late-time self-similar solutions

To demonstrate the time transition from early-time to late-time self-similarities, the location of the propagating front $\bar{x}_f(\bar{t})$ can be tracked based on the numerical solutions of PDE (12a), shown as the

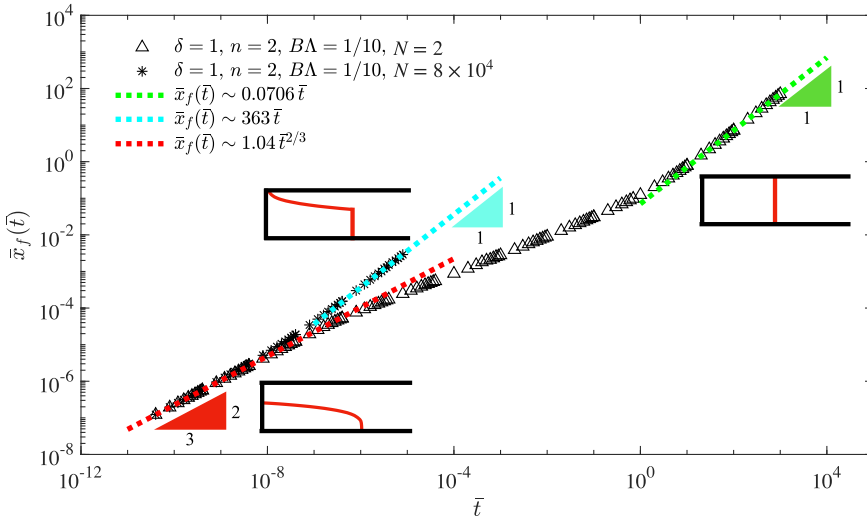


Figure 6. Time evolution of the frontal location $\bar{x}_f(\bar{t})$ from numerically solving PDE (12) and (18), imposing $\{\delta, n, B\Lambda, N\} = \{1, 2, 10^{-1}, 2\}$ and $\{\delta, n, B\Lambda, N\} = \{1, 2, 10^{-1}, 8 \times 10^4\}$. The profile shape evolves from an early-time capillary film towards either a compound-wave (for $N = 8 \times 10^4$) or a shock (for $N = 2$) at late times. The asymptotic solutions for the frontal location (33) and (33) are also included as the dashed lines.

symbols in Figure 6. For example, for $\{\delta, n, N, B\Lambda\} = \{1, 2, 8 \times 10^4, 10^{-1}\}$, the time-dependent location of the propagating front $\bar{x}_f(\bar{t})$ obeys the power-law form of

$$\bar{x}_f(\bar{t}) \sim 1.04 \bar{t}^{2/3} \quad \text{for } \bar{t} \ll 1, \tag{33a}$$

$$\bar{x}_f(\bar{t}) \sim 363 \bar{t} \quad \text{for } \bar{t} \gg 1, \tag{33b}$$

and for $\{\delta, n, N, B\Lambda\} = \{1, 2, 2, 1/10\}$, $\bar{x}_f(\bar{t})$ follows

$$\bar{x}_f(\bar{t}) \sim 1.04 \bar{t}^{2/3} \quad \text{for } \bar{t} \ll 1, \tag{34a}$$

$$\bar{x}_f(\bar{t}) \sim 0.0706 \bar{t} \quad \text{for } \bar{t} \gg 1. \tag{34b}$$

The PDE numerical solutions for $\bar{x}_f(\bar{t})$ can also be compared with the early-time and late-time self-similar solutions, shown as the dashed lines in Figure 6, and good agreement appears at both the early and late times. In the SM, we also compared the appropriately rescaled profile shapes from solving the original PDE system (12a), which further verifies the existence of these early-time and late-time asymptotes. A brief description of a finite volume scheme is also included in the SM that has been used to numerically solve the nonlinear advective-diffusive system.

2.4.2 Sharp-interface regime

When $B \gg 1$ or when $\Lambda \gg 1$, in contrast, analytical solution (13) for saturation field reduces to

$$s(\bar{x}, \bar{z}, \bar{t}) = \begin{cases} 1, & 0 \leq \bar{z} \leq \bar{h}(\bar{x}, \bar{t}), \\ 0, & \bar{h}(\bar{x}, \bar{t}) < \bar{z} \leq 1, \end{cases} \tag{35}$$

for any $\alpha \geq 0$ and $\beta \geq 0$, which represents an instantaneous change of fluid saturation $s(\bar{x}, \bar{z}, \bar{t})$ across a sharp interface $\bar{z} = \bar{h}(\bar{x}, \bar{t})$, as shown in Figure 2. The integrals $\bar{I}_s(\bar{h})$, $\bar{I}_n(\bar{h})$ and $\bar{I}_w(\bar{h})$ reduce to

$$\bar{I}_s(\bar{h}) \equiv \frac{\bar{h}^{2\delta/n+1}}{2\delta/n+1}, \quad \bar{I}_n(\bar{h}) = \frac{\bar{h}^{2\delta+1}}{2\delta+1} \quad \text{and} \quad \bar{I}_w(\bar{h}) = \frac{1 - \bar{h}^{2\delta+1}}{2\delta+1}. \tag{36a,b,c}$$

We can then study the early-time and late-time asymptotic solutions for the interface shape evolution in this sharp-interface regime and the time transition. A key message is that the existence of a vertical heterogeneity ($r_a(z) \sim r_1 z^\delta$) leads to a modification of the late-time interface shape from shock or rarefaction solutions (for $\delta = 0$) to compound-wave solutions. The frontal location of the invading fluid $\bar{x}_f(\bar{t})$ also adjusts accordingly. An interested reader can refer to the earlier reports of Zheng *et al.* (2015b) (for $\delta = 0$) and Hinton & Woods (2018) (for $\delta = 1/2$), where two more asymptotes are identified as unconfined gravity current flows at early times and confined interfacial flows at late times. We do not repeat the detailed descriptions here.

3. Potential implications

It is also of interest to briefly remark on the potential implications of the model and solutions. For example, in the context of geological CO₂ sequestration, it is important to understand the location of the propagating front and distribution of the supercritical CO₂, when a CO₂ plume is injected into a layer of saline aquifer. The correct result depends on the dominant physical mechanism that is related to the competition among the gravitational, pumping, and wetting and capillary forces, and the specific form of the heterogeneity of the porous layer. Quick insights can be obtained based on the value of the dimensionless parameters, and the characteristic time and length scales, imposing geophysical and operational parameters and fluids properties at reservoir conditions.

It has been shown in previous studies that for porous rocks with lower permeabilities, it is no longer appropriate to employ the sharp-interface flow models, as a CO₂ current can become significantly unsaturated due to the influence of the wetting and capillary effects (Golding *et al.* 2011; Zheng & Neufeld 2019). This is also true for the spreading of CO₂ currents in heterogeneous porous layers within regions of lower permeability, corresponding to pore sizes that are smaller than the capillary length scale. This is also demonstrated in cases (ii) and (iii) of the example calculations here with key features summarised in Table 2. It is assumed that a saline aquifer exhibits a linear variation in intrinsic permeability in the vertical direction in both cases (ii) and (iii), but the porous rock is more tight in case (iii) with much smaller pore sizes (and permeability). As a comparison, case (i) corresponds to the flow of CO₂ in an homogeneous layer with constant permeability, and the geophysical and operational parameters are consistent with those at the Sleipner sites. Details of the definition and physical meaning of the variables and dimensionless parameters can be found in the maintext.

In these example calculations, it has been illustrated that the rescaled buoyancy parameter $B \equiv \Delta\rho g r_1 h_0^{\delta+1} / \gamma \cos \theta$ can become relevant, based on the geophysical and operational parameters. Recall that B measures the competition between the gravitational and capillary forces for flow in heterogeneous porous layers, and the flow of CO₂ becomes unsaturated for moderate and small B . Since $1/B$ can also be understood as a rescaled length of the capillary fringe, physically, a small B indicates that the length of the capillary fringe now becomes comparable with the thickness of the porous layer h_0 . In such a situation, the CO₂ plume would distribute non-uniformly within the porous layer, and the saturation field would exhibit significant spatial variations. In this example, $B \approx 6.1$ in case (ii), while $B \approx 0.061$ in case (iii), leading to completely different flow regimes with either negligible or non-negligible capillary effects. It is likely to be reasonable to employ sharp-interface flow models to make prediction on the spreading dynamics of CO₂ for case (ii), while it is more appropriate to employ the unsaturated flow models for correct predictions for case (iii). We would stop the detailed discussions here by mentioning that the frontal location and saturation distribution of the CO₂ plume would adjust accordingly as injection proceeds. It is also important to remain aware that for the one-dimensional flow models to apply, the length of the current (with dimension) needs to be significantly greater than the height of the current, which must be checked eventually.

4. Summary and final remarks

We have provided a unified theory in this work for the gravity current, interfacial and unsaturated flows in a vertically heterogeneous porous layer, a model context that could find applications in geological CO₂

Table 2. Influence of vertical heterogeneity (δ) on the propagation of a CO₂ current in a layer of saline aquifer. The geophysical and operational properties are imposed based on the CO₂ sequestration project at the Sleipner site (Golding et al. 2011; Pegler et al. 2014; Guo et al. 2016a; Zheng & Neufeld 2019). We have imposed $\delta = 0$ in case (i) for an homogeneous porous layer and $\delta = 1/2$ in cases (ii) and (iii) for heterogeneous porous layers with a linearly varying permeability distribution ($k \propto z$), similar to previous investigations of sharp-interface flows (Huppert & Woods 1995; Hinton & Woods 2018). The geophysical parameters and fluid properties in case (i) are taken from those at the Sleipner site at reservoir conditions. By definition, $q \equiv Q/d$

Parameter	Description	Unit	Case (i)	Case (ii)	Case (iii)
δ	exponent in $r_a(z) = r_1 z^\delta$	[-]	0	1/2	1/2
r_1	prefactor in $r_a(z) = r_1 z^\delta$	[m ^{1-δ}]	4.90×10^{-6}	1.46×10^{-6}	1.46×10^{-8}
k_0	prefactor in $k(z) = k_0(r_1 z^\delta)^2$	[-]	1/12	1/12	1/12
ϕ_0	prefactor in $\phi(z) = \phi_0(r_1 z^\delta)^{2/n}$	[m ^{-2/n}]	7.35×10^4	7.35×10^4	7.35×10^6
n	exponent in $k(\phi) = k_n \phi^n$	[-]	2	2	2
Λ	exponent in $p_c/p_e = (1-s)^{-1/\Lambda}$	[-]	2	2	2
h_0	thickness of the porous layer	[m]	11.3	11.3	11.3
ρ_n	density of CO ₂	[kg m ⁻³]	760	760	760
ρ_w	density of salt water	[kg m ⁻³]	1020	1020	1020
μ_n	viscosity of CO ₂	[mPa·s]	0.06	0.06	0.06
μ_w	viscosity of salt water	[mPa·s]	0.80	0.80	0.80
g	gravitational acceleration	[m/s ²]	9.8	9.8	9.8
k_{rn0}	end-point relative permeability	[-]	0.116	0.116	0.116
S_r	residual saturation of salt water	[-]	0.11	0.11	0.11
γ	interfacial tension	[mN m ⁻¹]	30	30	30
θ	apparent contact angle	[deg]	40	40	40
Q	injection rate of CO ₂	[Mt yr ⁻¹]	1.0	1.0	1.0
d	length of horizontal well	[km]	4.1	4.1	4.1
$k(0)$	permeability at base ($z = 0$)	[mD]	2000	0	0
$k(h_0)$	permeability at cap ($z \rightarrow h_0^-$)	[mD]	2000	2000	0.2
$\phi(0)$	porosity at base ($z = 0$)	[-]	0.36	0	0
$\phi(h_0)$	porosity at cap ($z \rightarrow h_0^-$)	[-]	0.36	0.36	0.36
N	modified viscosity ratio	[-]	1.5	1.5	1.5
B	rescaled buoyancy force	[-]	6.1	6.1	0.061
x_c	characteristic length scale	[m]	143	143	0.014
t_c	characteristic time scale	[yr]	1.6	1.6	1.6×10^{-4}
	flow regime		interfacial	interfacial	unsaturated

sequestration, groundwater flow, pollutant transport, and oil and gas recovery. The theory presented in § 2 works for predominantly one-dimensional flows in porous systems with any form of vertical heterogeneity, in principle, providing that the assumption of vertical gravitational-capillary equilibrium continues to apply. We then impose power-law form of vertical heterogeneity to further demonstrate the concepts. Seven dimensionless parameters were identified, as summarised in Table 1: δ and n represent intrinsic features of vertical heterogeneity of the porous layer, α , β and Λ characterises multi-phase Darcy flow in homogeneous porous layers, N is the modified viscosity ratio, and B represents the competition between the gravitational and capillary forces. The influence of these dimensionless parameters (with an emphasis on δ and n) are then illustrated based on the asymptotic and numerical solutions of the saturation field, interface shape, and the frontal location.

In particular, when $B \ll 1$, the model predicts a significantly unsaturated flow regime (§ 2.4.1). A capillary film solution is identified at early times by solving a nonlinear diffusive equation, which evolves towards an unsaturated current solution at late times, with the profile shape described by either a shock or a compound-wave solution. Time transition between the early-time unconfined and late-time confined self-similar solutions is then demonstrated by tracking the interface shape and frontal location. In contrast, when $B \gg 1$ (or $\Lambda \gg 1$), the model predicts a sharp-interface flow regime (§ 2.4.2), when fluid saturation changes instantaneously across a sharp fluid–fluid interface, and a gravity current solution is identified at early times, which evolves towards a shock or compound-wave solution at late times (without considering the influence of buoyancy on the frontal structure). Finally, potential implications of the model and solutions are also demonstrated, using geophysical and operational parameters in the context of geological CO₂ sequestration in vertically heterogeneous porous layers.

Funding. We gratefully acknowledge funding by the Program for Professor of Special Appointment (Eastern Scholar, no. TP2020009) at Shanghai Institutions of Higher Learning.

Competing interests. The authors declare no conflict of interest.

Ethical statement. The research meets all ethical guidelines, including adherence to the legal requirements of the study country.

Data availability statement. Raw data are available from the corresponding author.

Supplementary material. The supplementary material for this article can be found at <https://doi.org/10.1017/flo.2025.13>.

References

- Al-Housseiny, T. T., Tsai, P. A., & Stone, H. A. (2012). Control of interfacial instabilities using flow geometry. *Nature Physics*, 8, 747–750.
- Boussinesq, J. V. (1904). Recherches theoretique sur l'ecoulement des nappes d'eau infiltrées dans le sol et sur le debit des sources. *Journal De Mathematiques Pures Et Appliquees*, 10, 5–78.
- Brooks, R. H., & Corey, A. T. (1964). Hydraulic properties of porous media. In *Hydrology Papers 3*. Colorado State University. Fort Collins, 1–27.
- Brusseau, M. L. (1995). The effect of nonlinear sorption on transformation of contaminants during transport in porous media. *Journal of Contaminant Hydrology*, 17, 277–291.
- Buckley, S. E., & Leverett, M. C. (1942). Mechanism of fluid displacement in sands. *Transactions of the AIME*, 146, 107–116.
- Cardoso, S. S. S., & Woods, A. W. (1995). The formation of drops through viscous instability. *Journal of Fluid Mechanics*, 289, 351–378.
- Ciriello, V., Di Federico, V., Archetti, R., & Longo, S. (2013). Effect of variable permeability on the propagation of thin gravity currents in porous media. *International Journal of Non-Linear Mechanics*, 57, 168–175.
- Coats, K. H., Dempsey, J. R., & Henderson, J. H. (1971). The use of vertical equilibrium in two-dimensional simulation of three-dimensional reservoir performance. *Society of Petroleum Engineers journal*, 11, 63–71.
- Dalwadi, M. P., Bruna, M., & Griffiths, I. M. (2016). A multi-scale method to calculate filter blockage. *Journal of Fluid Mechanics*, 809, 264–289.
- Dullien, F. A. L. (1992). *Porous media: Fluid transport and pore structure*. Academic Press.
- Golding, M. J., Huppert, H. E., & Neufeld, J. A. (2013). The effects of capillary forces on the axisymmetric propagation of two-phase, constant-flux gravity currents in porous media. *Physics of Fluids*, 25, 036602.
- Golding, M. J., Neufeld, J. A., Hesse, M. A., & Huppert, H. E. (2011). Two-phase gravity currents in porous media. *Journal of Fluid Mechanics*, 678, 248–270.
- Grenfell-Shaw, J. C., Hinton, E. M., & Woods, A. W. (2021). Instability of co-flow in a Hele-Shaw cell with cross-flow varying thickness. *Journal of Fluid Mechanics*, 927, R1.
- Gunn, I., & Woods, A. W. (2011). On the flow of buoyant fluid injected into a confined, inclined aquifer. *Journal of Fluid Mechanics*, 672, 109–129.
- Guo, B., Zheng, Z., Bandilla, K. W., Celia, M. A., & Stone, H. A. (2016a). Flow regime analysis for geologic CO₂ sequestration and other subsurface fluid injections. *International Journal of Greenhouse Gas Control*, 53, 284–291.
- Guo, B., Zheng, Z., Celia, M. A., & Stone, H. A. (2016b). Axisymmetric flows from fluid injection into a confined porous medium. *Physics of Fluids*, 28, 022107.
- Hesse, M. A., Tchelepi, H. A., Cantwell, B. J., & Orr, F. M. Jr. (2007). Gravity currents in horizontal porous layers: Transition from early to late self-similarity. *Journal of Fluid Mechanics*, 577, 363–383.

- Hinton, E. M., & Woods, A. W. (2018). Buoyancy-driven flow in a confined aquifer with a vertical gradient of permeability. *Journal of Fluid Mechanics*, *848*, 411–429.
- Hinton, E. M., & Woods, A. W. (2019). The effect of vertically varying permeability on tracer dispersion. *Journal of Fluid Mechanics*, *860*, 384–407.
- Huppert, H. E. (1982). The propagation of two-dimensional and axisymmetric viscous gravity currents over a rigid horizontal surface. *Journal of Fluid Mechanics*, *121*, 43–58.
- Huppert, H. E., & Woods, A. W. (1995). Gravity driven flows in porous layers. *Journal of Fluid Mechanics*, *292*, 55–69.
- Jackson, S. J., Agada, S., Reynolds, C. A., & Krevor, S. (2018). Characterizing drainage multiphase flow in heterogeneous sandstones. *Water Resources Research*, *54*, 3139–3161.
- Kowal, K., & Worster, M. G. (2015). Lubricated viscous gravity currents. *Journal of Fluid Mechanics*, *766*, 626–655.
- Kowal, K., & Worster, M. G. (2020). The formation of grounding zone wedges: Theory and experiments. *Journal of Fluid Mechanics*, *898*, A12.
- Longo, S., Ciriello, V., Chiapponi, L., & Di Federico, V. (2015). Combined effect of rheology and confining boundaries on spreading of porous gravity currents, advances in water resources. *Adv. Water Res.*, *79*, 140–152.
- MacMinn, C. W., Szulczewski, M. L., & Juanes, R. (2010). CO₂ migration in saline aquifers. Part 1. Capillary trapping under slope and groundwater flow. *Journal of Fluid Mechanics*, *662*, 329–351.
- Neufeld, J. A., Vella, D., & Huppert, H. E. (2009). The effect of a fissure on storage in a porous medium. *Journal of Fluid Mechanics*, *639*, 239–259.
- Nordbotten, J. M., & Celia, M. A. (2006). Similarity solutions for fluid injection into confined aquifers. *Journal of Fluid Mechanics*, *561*, 307–327.
- Paterson, L. (1981). Radial fingering in a Hele-Shaw cell. *Journal of Fluid Mechanics*, *113*, 513–529.
- Pegler, S., Kowal, K. N., Hasenclever, L. Q., & Worster, M. G. (2013). Lateral controls on grounding-line dynamics. *Journal of Fluid Mechanics*, *722*, R1.
- Pegler, S. S., Huppert, H. E., & Neufeld, J. A. (2014). Fluid injection into a confined porous layer. *Journal of Fluid Mechanics*, *745*, 592–620.
- Pegler, S., & Worster, M. G. (2013). An experimental and theoretical study of the dynamics of grounding lines. *Journal of Fluid Mechanics*, *728*, 5–28.
- Phillips, O. M. (1991). *Flow and reactions in permeable rocks*. Cambridge University Press.
- Pritchard, D., Woods, A. W., & Hogg, A. W. (2001). On the slow draining of a gravity current moving through a layered permeable medium. *Journal of Fluid Mechanics*, *444*, 23–47.
- Reyssat, M., Courbin, L., Reyssat, E., & Stone, H. A. (2008). Imbibition in geometries with axial variations. *Journal of Fluid Mechanics*, *615*, 335–344.
- Reyssat, M., Sangne, L. Y., Van Nierop, E. A., & Stone, H. A. (2009). Imbibition in layered systems of packed beads. *EPL*, *86*, 56002.
- Saffman, P. G., & Taylor, G. I. (1958). The penetration of a fluid into a porous medium or Hele-Shaw cell containing a more viscous fluid. *Proceedings of the Royal Society A*, *245*, 312–329.
- Seon, T., Znaeni, J., Salin, D., Hulin, J. P., Hinch, E. J., & Perrin, B., (2007). Transient buoyancy-driven front dynamics in nearly horizontal tubes. *Physics of Fluids*, *19*, 123603.
- Zheng, Z. (2022). Upscaling unsaturated flows in vertically heterogeneous porous layers. *Journal of Fluid Mechanics*, *950*, A17.
- Zheng, Z., Christov, I. C., & Stone, H. A. (2014). Influence of heterogeneity on second-kind self-similar solutions for viscous gravity currents. *Journal of Fluid Mechanics*, *747*, 218–246.
- Zheng, Z., Guo, B., Christov, I. C., Celia, M. A., & Stone, H. A. (2015a). Flow regimes for fluid injection into a confined porous medium. *Journal of Fluid Mechanics*, *767*, 881–909.
- Zheng, Z., & Neufeld, J. A. (2019). Self-similar dynamics of two-phase flows injected into a confined porous layer. *Journal of Fluid Mechanics*, *877*, 882–921.
- Zheng, Z., Ronge, L., & Stone, H. A. (2015b). Viscous fluid injection into a confined channel. *Physics of Fluids*, *27*, 062105.
- Zheng, Z., Soh, B., Huppert, H. E., & Stone, H. A. (2013). Fluid drainage from the edge of a porous reservoir. *Journal of Fluid Mechanics*, *718*, 558–568.